



# Dielectric temperature stability and energy storage performance of B-site Sn<sup>4+</sup>-doped BNKBST ceramics

Guangzhi Dong<sup>1,2</sup> · Huiqing Fan<sup>1</sup> · Yuxin Jia<sup>1</sup> · Huan Liu<sup>1</sup>

Received: 28 April 2020 / Accepted: 30 June 2020 / Published online: 9 July 2020  
© Springer Science+Business Media, LLC, part of Springer Nature 2020

## Abstract

The 0.65Bi<sub>0.5</sub>Na<sub>0.25</sub>K<sub>0.25</sub>TiO<sub>3</sub>–0.35Bi<sub>0.2</sub>Sr<sub>0.7</sub>Ti<sub>1–x</sub>Sn<sub>x</sub>O<sub>3</sub> (BNKBST-*x*Sn) ceramics were synthesized via a solid-phase reactive sintering technique. The effects of doping Sn<sup>4+</sup> ions on the energy storage, dielectric, ferroelectric properties and microstructure characteristics for BNKBST ceramics were systematically studied. Remarkably, BNKBST-0.02Sn exhibits a superior dielectric temperature stability, manifested as the change rate for dielectric constant  $\Delta\epsilon/\epsilon_{150^\circ\text{C}}$  is smaller than 15% during a very wide temperature range of 30–400 °C. In addition, BNKBST-0.02Sn ceramic achieves a high energy storage density  $W_{\text{rec}} = 0.81 \text{ J/cm}^3$  (under the electric field 80 kV/cm) with an outstanding energy storage efficiency 89.5%, which make it reasonable to be applied in dielectric capacitors due to its excellent dielectric thermal stability and energy storage properties. The electrical conductivity behaviors of BNKBST-*x*Sn were also analyzed with the assistance of impedance spectroscopy.

## 1 Introduction

Dielectric capacitor is pivotal component in electronic equipment due to its excellent power density property which can generate high power [1, 2]. However, the dielectric capacitors often exhibit inferior energy storage density which restricts the integration of electronic equipment [3, 4]. Therefore, it is urgent to prepare high-quality dielectric material with excellent energy storage density performance to satisfy the requirements of pulse capacitors. Currently, the dielectric energy storage materials could be roughly divided to four kinds: antiferroelectrics [5–8], glass ceramics [9–11], relaxor ferroelectrics [12–16], and polymer-based ferroelectrics [17, 18], which are considered to be applied into the next-generation dielectric capacitor. Among these energy storage systems, relaxor ferroelectrics have attracted extensive attention because of their low remnant polarization, low loss, and nonlinear characteristics. According to the equation of the energy storage density ( $J = \int E dP$ ) [19], a large

maximum polarization ( $P_{\text{max}}$ ), a small remnant polarization ( $P_r$ ), and combined with a high dielectric breakdown field strength (DBS) are required to achieve enhanced energy storage property.

Bi<sub>0.5</sub>Na<sub>0.5</sub>TiO<sub>3</sub> (BNT) exhibits a high  $P_{\text{max}}$  of 43  $\mu\text{C/cm}^2$  due to its excellent ferroelectric performance, which makes it a promising energy storage candidate material [20–27]. Hence a concomitant high remnant polarization of 39  $\mu\text{C/cm}^2$ , a large coercive field ( $E_C$ ), and a high leakage current are shown in pure BNT. So, it is necessary to reduce the  $P_r$  and enhance the DBS to enhance the energy storage property of BNT-based systems. Similar to BaTiO<sub>3</sub> (BT)-based systems [28–34], it is a classical way to design a binary or ternary solid solution by introducing other perovskite system into BNT system to form relaxor ferroelectric [35–39]. Among them, Bi<sub>0.5</sub>Na<sub>0.5</sub>TiO<sub>3</sub>–Bi<sub>0.2</sub>Sr<sub>0.7</sub>TiO<sub>3</sub> (BNBST) binary system is a good relaxor ferroelectric [40, 41], which make it a good candidate composition for further chemical modification.

In this work, Sn<sup>4+</sup> ion-doped 0.65Bi<sub>0.5</sub>Na<sub>0.25</sub>K<sub>0.25</sub>TiO<sub>3</sub>–0.35Bi<sub>0.2</sub>Sr<sub>0.7</sub>Ti<sub>1–x</sub>Sn<sub>x</sub>O<sub>3</sub> (BNKBST-*x*Sn) ceramics were designed and synthesized. The influences of B-site Sn<sup>4+</sup> ion modification on the morphology, microstructure, ferroelectric, dielectric, energy storage properties, and conductivity behaviors were studied systematically.

✉ Huiqing Fan  
hqfan3@163.com

<sup>1</sup> State Key Laboratory of Solidification Processing, School of Materials Science and Engineering, Northwestern Polytechnical University, Xi'an 710072, China

<sup>2</sup> Institute for Superconducting and Electronic Materials, Australia Institute of Innovative Materials, University of Wollongong, Wollongong 2522, Australia

## 2 Experimental process

$\text{Sn}^{4+}$ -doped  $0.65\text{Bi}_{0.5}\text{Na}_{0.25}\text{K}_{0.25}\text{TiO}_3-0.35\text{Bi}_{0.2}\text{Sr}_{0.7}\text{Ti}_{1-x}\text{Sn}_x\text{O}_3$  (BNKBST- $x\text{Sn}$ ,  $x=0, 0.02, 0.05, 0.08$ ) solid solutions were synthesized by a solid-phase sintering technique, and the experimental flow chart is shown in Fig. 1. The raw materials for the experiment are  $\text{Bi}_2\text{O}_3$  (99.99%),  $\text{Na}_2\text{CO}_3$  (99.6%),  $\text{K}_2\text{CO}_3$  (99.0%),  $\text{TiO}_2$  (98%),  $\text{SrCO}_3$  (99%), and  $\text{SnO}_2$  (99%), which are all provided by SinoReagent. First, raw powders were weighed accurately according to the designed proportion. They were then mixed by a ball-milling with ethanol as grinding aid. Subsequently, the slurries were poured out and dried. The obtained powders were calcined, and the second milling was performed. Then the dried powders were mold pressed into pellets for sintering.

X-ray diffractometer (XRD; X'Pert PRO MPD, Philips, Eindhoven, The Netherlands) was utilized to determine phase structure. Microstructures in detail were checked using a scanning electron microscope (SEM; JSM-5610, JEOL, Tokyo, Japan). An electrochemical workstation (CHI660E, CH Instruments, Shanghai, China) was applied in testing the impedance data for unpoled ceramics. The polarization versus electric field ( $P$ - $I$ - $E$ ) curves were collected using a ferroelectric analyzer (TF-2000, aixACCT, Aachen, Germany). An impedance analyzer (4294 A, Agilent, SantaClara, CA, USA) was used to detect dielectric parameters from 25 to 450 °C.

## 3 Results and discussion

Figure 2 displays the power XRD patterns of BNKBST- $x\text{Sn}$  samples at room temperature (RT). We can find that the diffraction peaks of all ceramic samples with different compositions appear in the same position without obvious deviation. It suggests that each sample is composed of a single phase, without formation of new impurity phase. Therefore, XRD results suggest that  $\text{Sn}^{4+}$  ions have diffused in the BNKBST cell structure. In addition, the position of XRD diffraction peaks of all samples does not change significantly, indicating

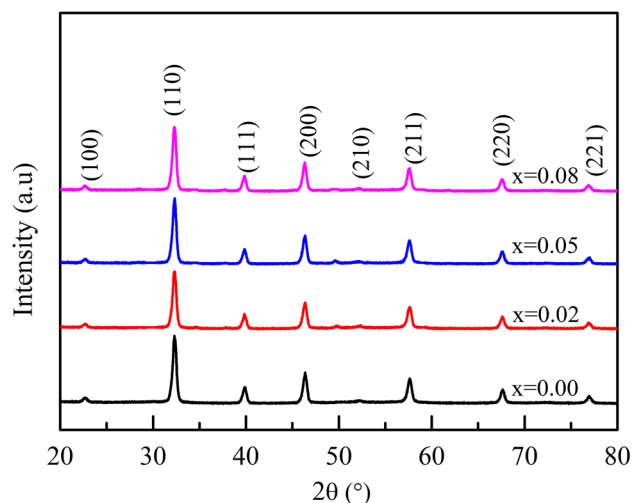


Fig. 2 RT XRD patterns of as-prepared BNKBST- $x\text{Sn}$

that the content of  $\text{Sn}^{4+}$  ions did not obviously affect the lattice parameters of BNKBST ceramics. Since the absence of the peaks splitting, the BNKBST- $x\text{Sn}$  exhibit the pseudocubic structure.

SEM micrographs of BNKBST- $x\text{Sn}$  ceramics are shown in Fig. 3, indicating that all samples exhibit homogeneous surface micromorphology with clear grain boundaries between the grains. As the content of doped  $\text{Sn}^{4+}$  ions increase, the surface micromorphology of the ceramics become more compact and uniform. The insets in Fig. 3 display the histogram of grain size distribution, and the average grain size decreases slightly with the increase of doping content. The abnormal growth of crystal grains is suppressed after introducing a certain amount of  $\text{Sn}^{4+}$  ions at the B-site, which is also reflected in the increase of relative density, which is 95%, 96%, 98%, and 98% for the four compositions, respectively.

Figure 4 reveals the temperature dependence of dielectric permittivity ( $\epsilon'$ ) and loss ( $\tan\delta$ ) for BNKBST- $x\text{Sn}$  specimens during a temperature range from RT to 400 °C with the test frequency at 1 kHz, 10 kHz, 100 kHz. It can be seen from Fig. 4 that as increase of  $\text{Sn}^{4+}$  content, the dielectric constant

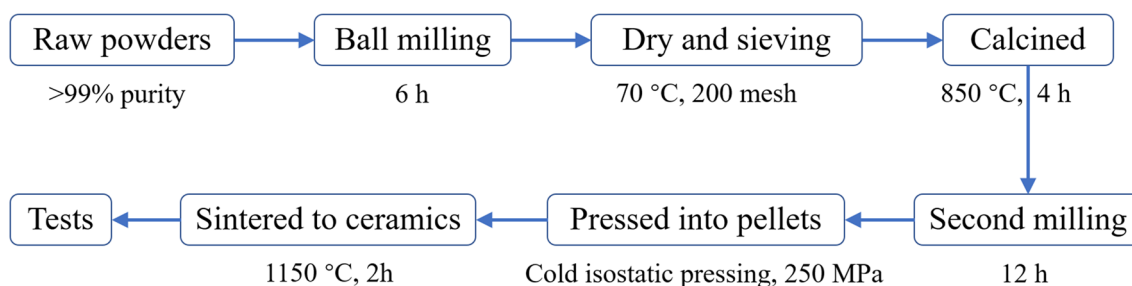
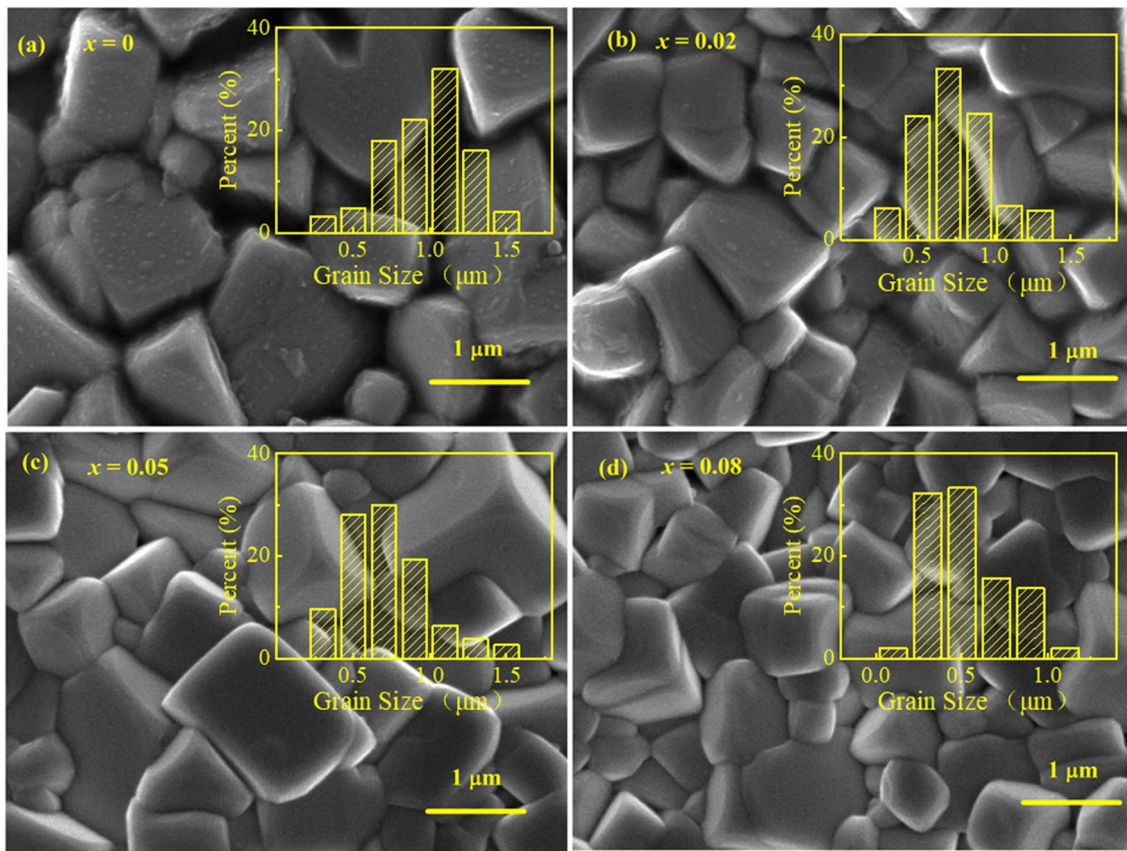


Fig. 1 Experimental flow-chart for fabricating BNKBST- $x\text{Sn}$  ceramics



**Fig. 3** SEM images and grain size distributions (insets) of BNKBST- $x$ Sn

decreases slightly and the dielectric relaxation behavior increases. It can also be obtained that when the temperature exceeds 300 °C, the dielectric loss increases rapidly, which is related to the thermal activation process of carriers. In addition, two dielectric anomaly peaks exist on all  $\epsilon'$ - $T$  plots, marked as  $T_S$  and  $T_m$ . Frequency dispersion can also be observed obviously near the peaks. The first  $T_S$  peak shifts toward to high temperature with the increasing of frequency, while the second dielectric peak hardly changes, indicating that the two dielectric peaks have different dispersion mechanisms. The first dielectric peak is usually considered to be related with the heat activation process of rhombohedral and tetragonal polar nanoregions (PNRs) [42]. The  $T_m$  peak is attributed to a phase transition process, which indicates the tetragonal high-temperature polar nanoregions begin to appear during the cooling process [43]. The loss tangent  $\tan\delta$  curves exhibit high loss values and significant relaxation phenomenon at around  $T_S$  temperature, which is due to the competition between rhombohedral and tetragonal polar nanoregions. The  $\tan\delta$  decreases at around  $T_m$  temperature, indicating the phase has transformed to high symmetry.

Figure 5 displays the plots of  $\ln(1/\epsilon - 1/\epsilon_m)$  vs.  $\ln(T - T_m)$  of BNKBST- $x$ Sn specimens under the frequency of 1 kHz.

The modified Curie–Weiss relation can be utilized to calculate the degree of relaxation characteristic, shown as follows [36]:

$$\frac{1}{\epsilon} - \frac{1}{\epsilon_m} = \frac{(T - T_m)^\gamma}{C} \quad (1)$$

where  $\gamma$  is the dielectric relaxation factor ( $1 \leq \gamma \leq 2$ ), and  $\epsilon_m$  is the maximum dielectric constant. Generally, for typical ferroelectric materials, the dielectric relaxation factor  $\gamma$  equals to 1. When the material is transformed into a relaxor ferroelectric, the value of  $\gamma$  will increase to around 2. The relationship for  $\ln(1/\epsilon - 1/\epsilon_m)$  and  $\ln(T - T_m)$  is linear for all BNKBST- $x$ Sn samples, and the dielectric relaxation factors of all components are calculated to be approach to 2, indicating the phase transition occurring at high temperature is a relaxation process.

The temperature stability of the dielectric permittivity during a wide temperature range is a very important indicator to measure the quality of dielectric ceramic capacitors [44–47]. Usually, 150 °C can be used as the reference temperature of high-temperature capacitor, using  $\Delta\epsilon/\epsilon_{150^\circ\text{C}}$  to characterize the stability of the dielectric constant of

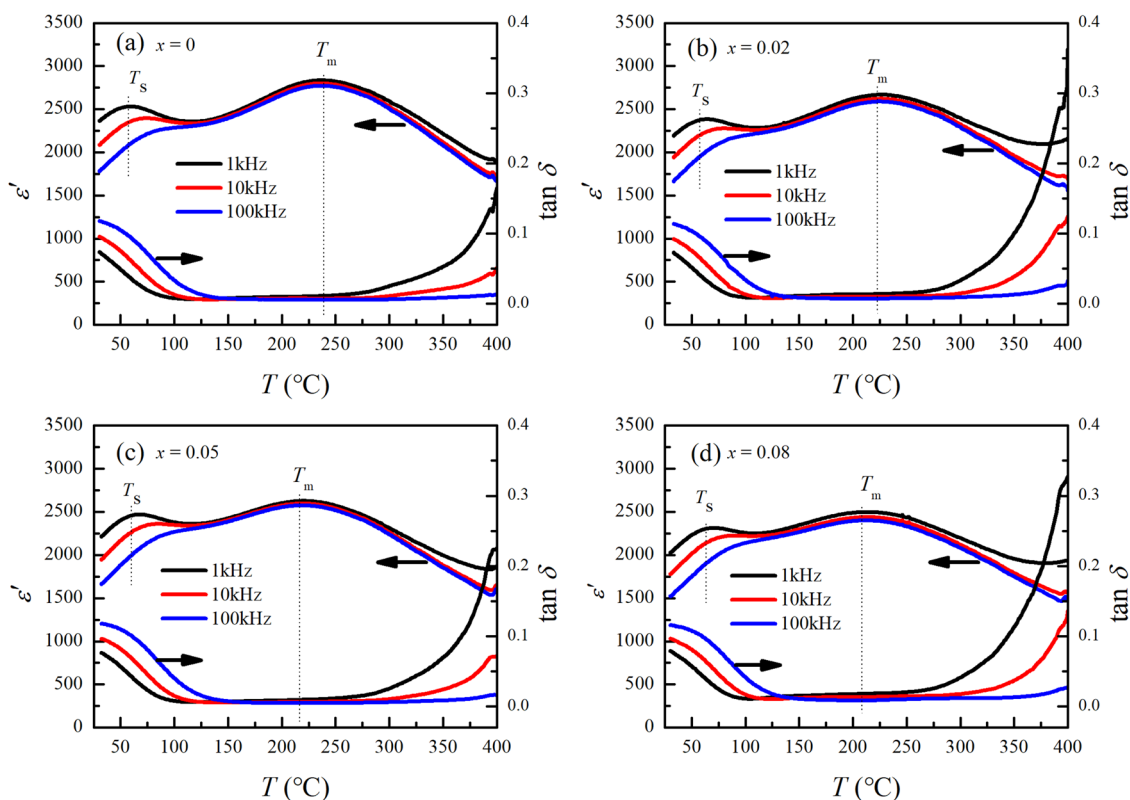


Fig. 4 Temperature-dependent dielectric permittivity and loss of BNKBST-*x*Sn

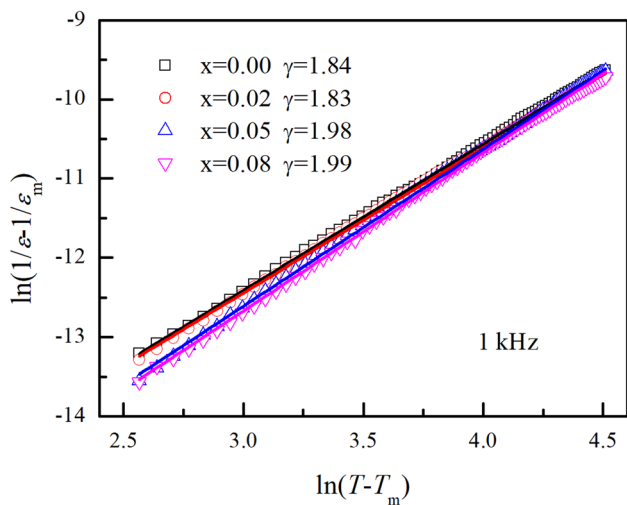


Fig. 5 The modified Curie–Weiss fit shows a dielectric relaxation factor of  $\sim 2$  for all the samples, indicating the ceramic is a relaxor ferroelectric

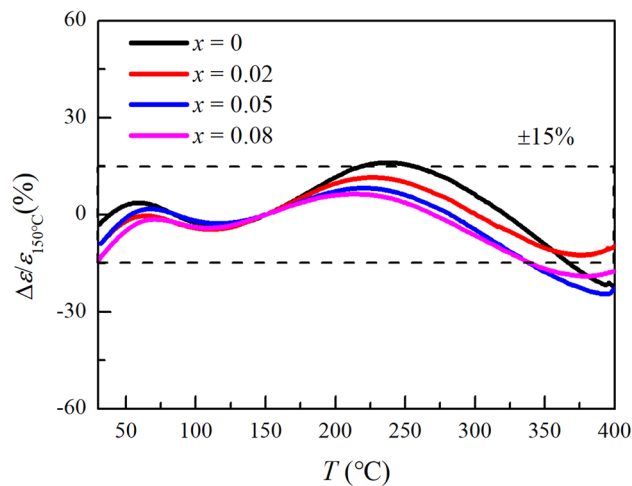


Fig. 6 The temperature stable dielectric properties of BNKBST-*x*Sn ceramics

materials. The temperature dependence of  $\Delta\epsilon/\epsilon_{150^\circ\text{C}}$  curves for BNKBST-*x*Sn ceramics over the entire measurement temperature range at a frequency of 1 kHz is shown in Fig. 6. The dotted frame in the figure represents the temperature range with a change rate of 15%. It can be

concluded that with the increase of doped  $\text{Sn}^{4+}$  ions, the temperature stability range widens gradually. At the composition of  $x=0.02$ , the dielectric permittivity is steady in a very wide range (RT  $\sim$  400 °C), while the  $\epsilon'$  at 150 °C is as high as 2390, and the dielectric loss is only 1.1%.

The comparison of dielectric temperature stability between BNKBST-0.02Sn ceramic and other similar ceramic systems is displayed in Table 1. Compared with other systems, BNKBST-0.02Sn ceramic has wider dielectric temperature stability and lower dielectric loss, which means BNKBST-0.02Sn ceramic possess potential application prospects in the field of ceramic capacitors.

Figure 7 exhibits the electric-induced ferroelectric and current ( $P$ - $I$ - $E$ ) curves of BNKBST- $x$ Sn ceramics under

**Table 1** Comparison of the temperature stable dielectric performance of BNKBST-0.02Sn to other ceramic systems

Samples	Ref.	Temperature range (°C)	$\tan\delta$ (%)	$\epsilon'$ (150 °C)
BNT-BCZT-0.1KNN	[48]	66–450	1.3	1633
BNT-BST-0.15KN	[49]	30–297	0.3	3484
BNT-BT-0.15CZ	[50]	52–490	3	946
BZN-0.97KNN	[51]	100–400	2	2000
BNT-BT-0.15KNN	[52]	40–330	2	2349
BNKT-BST-0.02Sn	This work	30–400	1.1	2390

electric field of 70 kV/cm at RT. It can be clearly seen from the ferroelectric hysteresis curves that the loops of all samples are slim, with low remnant polarization  $P_r$  (lower than  $0.5 \mu\text{C}/\text{cm}^2$ ), indicating that all samples exhibit the features of typical relaxor ferroelectrics. As the content of  $\text{Sn}^{4+}$  ions increase, the  $P_{\text{max}}$  decrease slightly, while  $P_r$  remain almost unchanged. These changes indicate that the introduction of  $\text{Sn}^{4+}$  ions suppresses the transformation of polar nanoregions to ferroelectric domains by applying the external electric field, leading to the suppression of ferroelectricity.

As shown in Fig. 7, there arises four current peaks in the  $I$ - $E$  loops for all BNKBST- $x$ Sn samples. The generation of current peak corresponds the transformation between polar nanoregions and ferroelectric domains under the electric field. The polar nanoregions gradually grow to ferroelectric domains by increasing the electric field, and the orientation of the polar regions becomes consistent with the orientation of external field. By contrast, as the electric field decreases, the directional arrangement of the domains slowly disappears, indicating the presentation of phase transformation from ferroelectric to ergodic relaxor phase. With more  $\text{Sn}^{4+}$  ions doped, the current peak gradually becomes smoother and shifts slightly towards the high electric field, indicating that the introduction of  $\text{Sn}^{4+}$  ions leads to the suppression of the phase transitions.

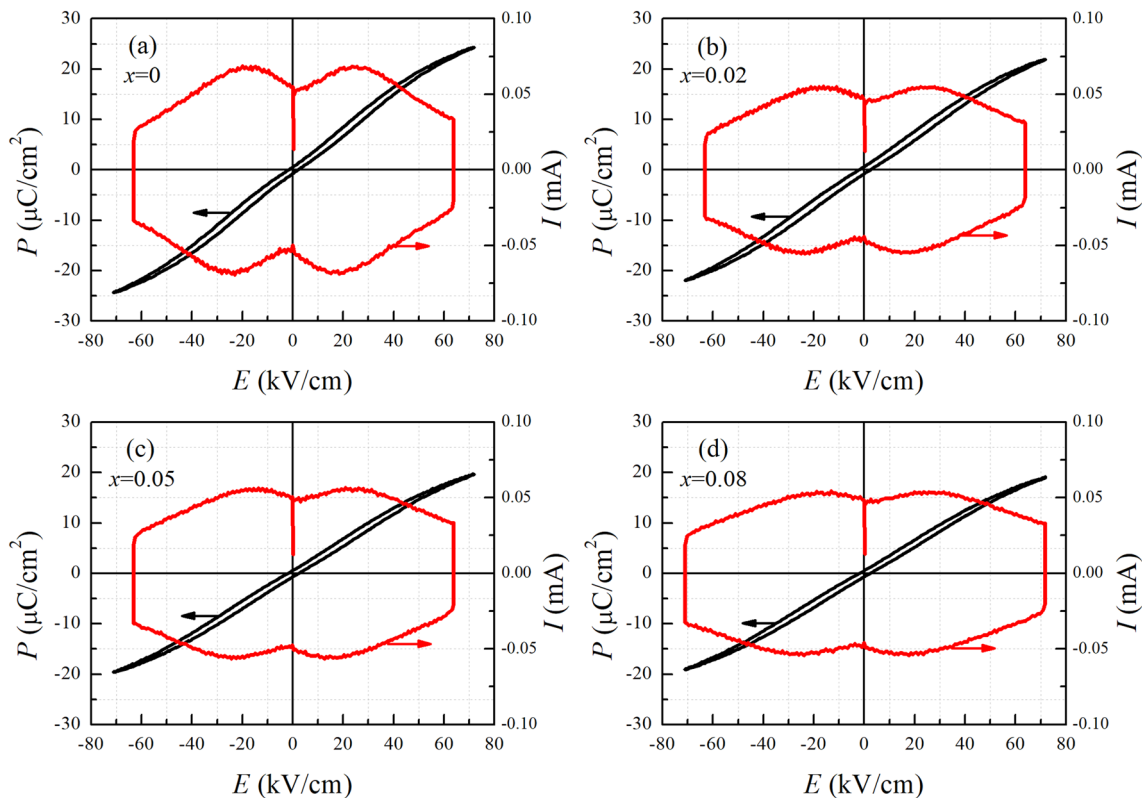


**Fig. 7** The electric-induced ferroelectric and current curves of BNKBST- $x$ Sn

The effective energy storage density  $W_{rec}$ , total energy storage density  $W$ , and energy storage efficiency  $\eta$  of BNKBST- $x$ Sn samples under the electric field of 70 kV/cm are calculated and shown in Fig. 8. Obviously, as  $Sn^{4+}$  ions increase, the energy storage density for BNKBST- $x$ Sn ceramics decreases continuously, which is mainly due to the

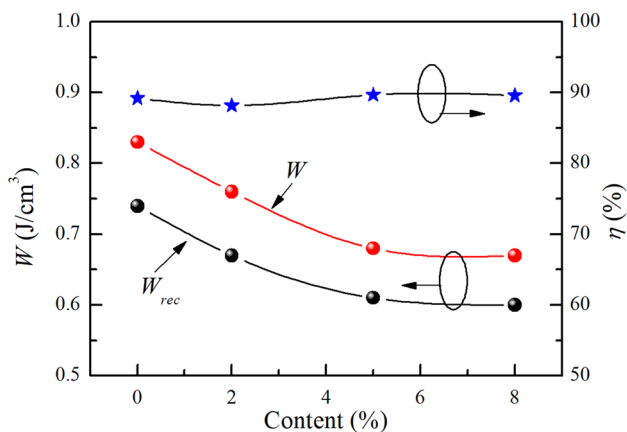


Fig. 8 Energy storage densities and efficiencies of BNKBST- $x$ Sn

decrease in the  $P_{max}$  of the samples. Nevertheless, the energy storage efficiency is almost unchanged (around 90%), indicating the low energy losses during the energy storage and application process, which benefits from the small hysteresis behavior contributed by the small  $Pr$  values of  $P$ - $E$  loops.

Figure 9a shows the complex impedance spectra of BNKBST-0.02Sn ceramic as representative in operating temperature range of 500–700 °C. Generally, the AC complex impedance data can be simulated with an equivalent circuit consisted with three RC components, corresponding to electrode, grain boundary, and grain from low frequency to high frequency, respectively. As shown in Fig. 9a, the curve at each temperature appears as a semicircle (Debye semicircle), which indicates that only one element affects the conductance of BNKBST-0.02Sn, namely the grain effect. The diameter of the impedance semicircle decreases as the temperature increases, and the bulk conductivity of the sample can be obtained by fitting the diameter of the Debye semicircle.

The normalized imaginary part of impedance spectra ( $Z''/Z''_{max}$ ) as a function of frequency is shown in Fig. 9b. There is only one peak in each curve. As the temperature increases, the peak gradually moves toward the high

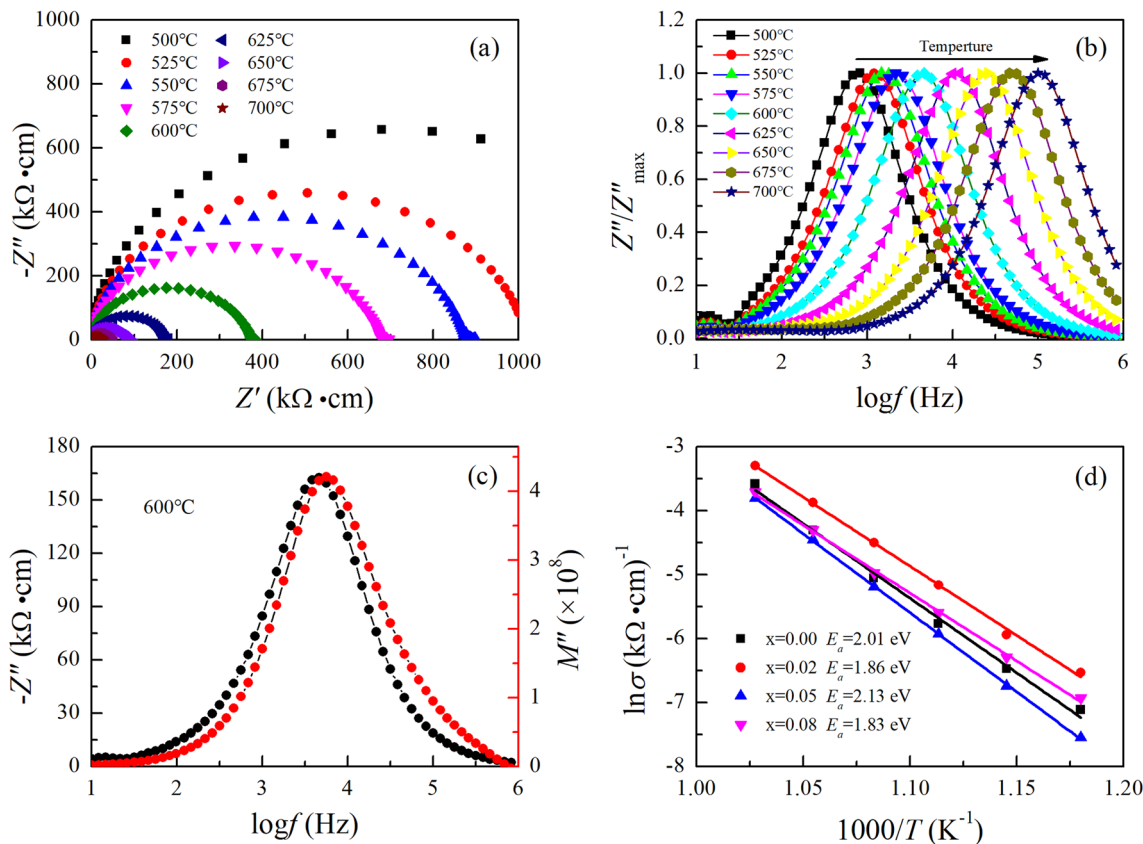


Fig. 9 **a** Complex impedance plots at 540–720 °C, **b** frequency dependence of impedance plots at 540–720 °C, and **c** frequency dependence of impedance  $Z''$  and electric modulus  $M''$  at 600 °C for BNKBST-0.02Sn; **d** Arrhenius fitting of activation energy for BNKBST- $x$ Sn

frequency. This suggests that the temperature-dependent relaxation characteristic is associated with the existence of defects or oxygen vacancies in the BNKBST-0.02Sn ceramic. Generally, long-range migration of oxygen vacancies can only occur at the frequency below the  $Z''$  peak. In the frequency range higher than the  $Z''$  peak, ions and oxygen vacancies can only migrate within a short distance.

Figure 9c reveals the frequency dependence for the normalized imaginary part of impedance  $Z''$  and electric modulus  $M''$  under 600 °C. Only one peak can be observed in the frequency dependent  $Z''$  and  $M''$  spectra. The two plots almost overlap, and the two peaks appear at a similar frequency. This can be explained by the fact that the conductance mechanism of BNKBST-0.02Sn ceramic is mainly dominated by the grain effect in the test frequency range.

In general, the activation energy  $E_a$  is used to indicate the concentration of oxygen vacancies in samples. In order to further reveal the relation of defects and dielectric relaxation behaviors,  $E_a$  is calculated by the Arrhenius law [53]:

$$\sigma = \sigma_c \exp\left(\frac{E_a}{kT}\right).$$

where  $\sigma$  means the conductivity calculated from the fitted impedance spectrum,  $k$  is the Boltzmann constant and  $\sigma_c$  refers to the pre-factor. Figure 9d is the relationship between  $\ln\sigma$  and  $1000/T$  of BNKBST- $x$ Sn ceramic at the temperature of 500–700 °C. As represented in Fig. 8d, the calculated  $E_a$  values of BNKBST- $x$ Sn ceramics are in the range of 1.83–2.13 eV, which is close to that of oxygen vacancy migration. Since all ceramic samples have similar  $E_a$  values, indicating that they have the similar energy barriers and same conductance mechanism.

## 4 Conclusions

In summary, the novel BNKBST- $x$ Sn ceramics were synthesized via a traditional solid-phase reaction sintering method in this work, and the dielectric temperature stability, ferroelectric properties, and energy storage characteristics were systematically studied. After doping  $\text{Sn}^{4+}$  ions, BNKBST ceramic still maintains the original perovskite structure, but the relaxation behavior is significantly enhanced. As the doping contents of  $\text{Sn}^{4+}$  increase, the dielectric peak becomes wider. Especially, the dielectric constant of BNKBST-0.02Sn ceramic at 150 °C reaches 2390, with the dielectric loss of only 1.1%. The rate of change for dielectric permittivity around 150 °C in the wide temperature range of 30–400 °C is less than 15%, meaning that it has good dielectric temperature stability. In spite of the fact that the maximum polarization reduces with the remnant polarization unchanged as the increase of  $\text{Sn}^{4+}$  ions, the breakdown

field strength of ceramics increases due to the decrease of the grain sizes, thereby improving the energy storage performance of the ceramic. The BNKBST-0.02Sn composition reaches the maximum energy storage density  $W_{\text{rec}} = 0.81 \text{ J/cm}^3$  (under 80 kV/cm) with a high energy storage efficiency  $\eta$  equals to 89.5%. The impedance data analysis shows that the conductance response of BNKBST- $x$ Sn ceramics are determined by the grain response. The calculated activation energy suggests that the resistance of the ceramics and the internal defect mechanism are mainly caused by oxygen vacancies.

**Acknowledgements** This work has been supported by the National Natural Science Foundation (51672220, 51902258), Fundamental Research Funds for the Central Universities of NPU (3102019GHXM002), State Key Laboratory of Solidification Processing Project (2019-TZ-04) of China, China Postdoctoral Science Foundation (2019M653729), Shaanxi Province Postdoctoral Science Foundation (2017BSHEDZZ07), and the Natural Science Foundation of Shaanxi Province (2019JQ-621). We would also like to thank the Analytical & Testing Center of Northwestern Polytechnical University.

## References

1. G.R. Love, *J. Am. Ceram. Soc.* **73**, 323 (1990)
2. X.H. Hao, *J. Adv. Dielectr.* **3**, 1330001 (2013)
3. Z.H. Yao, Z. Song, H. Hao, Z.Y. Yu, M.H. Cao, S.J. Zhang, M.T. Lanagan, H.X. Liu, *Adv. Mater.* **29**, 1601727 (2017)
4. Q. Li, F.Z. Yao, Y. Liu, G. Zhang, H. Wang, Q. Wang, *Ann. Rev. Mater. Res.* **48**, 219 (2018)
5. L. Zhao, Q. Liu, J. Gao, S.J. Zhang, J.F. Li, *Adv. Mater.* **29**, 1701824 (2017)
6. H. Qi, R.Z. Zuo, A.W. Xie, A. Tian, J. Fu, Y. Zhang, S.J. Zhang, *Adv. Funct. Mater.* **29**, 1903877 (2019)
7. H.S. Wang, Y.C. Liu, T.Q. Yang, S.J. Zhang, *Adv. Funct. Mater.* **29**, 1807321 (2019)
8. S.F. Mao, N.N. Luo, K. Han, Q. Feng, X.Y. Chen, B.L. Peng, L.J. Liu, C.Z. Hu, H.F. Zhou, F. Toyohisa, Y.Z. Wei, *J. Mater. Sci.* (2020). <https://doi.org/10.1007/s10854-020-03309-7>
9. Y. Zhang, J.J. Huang, T. Ma, X.R. Wang, C.S. Deng, X.M. Dai, *J. Am. Ceram. Soc.* **94**, 1805 (2011)
10. S.X. Xue, S. Xiao, J.W. Zhai, *J. Mater. Sci.-Mater. Electron.* **29**, 16758 (2018)
11. B. Li, D.Z. Wang, G.H. Chen, X. Liu, C.L. Yuan, *J. Mater. Sci.-Mater. Electron.* **30**, 19262 (2019)
12. T. Wang, L. Jin, C.C. Li, Q.Y. Hu, X.Y. Wei, *J. Am. Ceram. Soc.* **98**, 559 (2015)
13. Q.B. Yuan, G. Li, F.Z. Yao, S.D. Cheng, Y.F. Wang, R. Ma, S.B. Mi, M. Gu, K. Wang, J.F. Li, H. Wang, *Nano Energy* **52**, 203 (2018)
14. X. Liu, J. Shi, F.Y. Zhu, H.L. Du, T.Y. Li, X.C. Liu, H. Lu, *J. Mater. Sci.* **4**, 202 (2018)
15. X.L. Chen, X. Li, H.F. Zhou, J. Sun, X.X. Li, X. Yan, C.C. Sun, J.P. Shi, F.H. Pang, *J. Mater. Sci.-Mater. Electron.* **30**, 15912 (2019)
16. C. Wang, N.N. Sun, X.H. Hao, *J. Mater. Sci.-Mater. Electron.* **31**, 2063 (2020)
17. Z. Wang, W.W. Nian, T. Wang, Y.J. Xiao, H.N. Chen, *J. Mater. Sci.-Mater. Electron.* **29**, 9129 (2018)
18. Z. Zhang, H. Yang, H. Wang, X.G. Ding, Q.L. Zhang, Z.C. Zhu, *J. Mater. Sci.-Mater. Electron.* **30**, 2501 (2019)

19. Q.L. Zhao, H. Lei, G.P. He, J.J. Di, D.W. Wang, P.P. Tan, H.B. Jin, M.S. Cao, *Ceram. Int.* **42**, 1314 (2016)
20. J. Yin, Y.X. Zhang, X. Lv, J.G. Wu, *J. Mater. Chem. A* **6**, 9823 (2018)
21. P.R. Ren, J.J. He, X. Wang, Y.H. Wan, F.X. Yan, G.Y. Zhao, *J. Mater. Sci.-Mater. Electron.* **29**, 17016 (2018)
22. P.R. Ren, Z.C. Liu, X. Wang, Z.F. Duan, Y.H. Wan, F.X. Yan, G.Y. Zhao, *J. Alloys Compd.* **742**, 683 (2018)
23. P.R. Ren, J.J. He, L. Sun, T. Frömling, Y.H. Wan, S. Yang, X.H. Cao, B.Y. Wang, *J. Eur. Ceram. Soc.* **39**, 4160 (2019)
24. P. Chen, L.Y. Zhang, J. Cai, Z.Y. Wang, W.J. Shi, J.J. Jing, F.B. Wei, G. Liu, Y. Yan, H.B. Liu, L. Jin, *J. Mater. Sci.-Mater. Electron.* **30**, 13556 (2019)
25. B. Wang, Y.P. Pu, Q.B. Yuan, C.W. Cui, G.D. Shen, *J. Mater. Sci.-Mater. Electron.* **30**, 12950 (2019)
26. H.L. Lian, R.X. Cheng, Y.Z. Qiu, J.Y. Shi, X.M. Chen, *J. Mater. Sci.-Mater. Electron.* **31**, 7927 (2020)
27. Y.B. Sun, H. Wang, G.B. Liu, H. Xie, C.R. Zhou, G.H. Chen, C.L. Yuan, J.W. Xu, *J. Mater. Sci.-Mater. Electron.* **31**, 5546 (2020)
28. G. Wang, Z.L. Lu, J.L. Li, H.F. Ji, H.F. Yang, L.H. Li, S.K. Sun, A. Feteira, H.G. Yang, R.Z. Zuo, D.W. Wang, I.M. Reaney, *J. Eur. Ceram. Soc.* **40**, 1779 (2020)
29. G. Wang, J.L. Li, X. Zhang, Z.M. Fan, F. Yang, A. Feteira, D. Zhou, D.C. Sinclair, T. Ma, X.L. Tan, D.W. Wang, I.M. Reaney, *Energy Environ. Sci.* **12**, 582 (2019)
30. G. Liu, Y. Li, M.Q. Shi, L.J. Yu, P. Chen, K. Yu, Y. Yan, L. Jin, D.W. Wang, J.H. Gao, *Ceram. Int.* **45**, 19189 (2019)
31. W.B. Li, D. Zhou, R. Xu, D.W. Wang, J.Z. Su, L.X. Pang, W.F. Liu, G.H. Chen, *A.C.S. Appl. Energy Mater.* **2**, 5499 (2019)
32. D.W. Wang, Z.M. Fan, D. Zhou, A. Khesro, S. Murakami, A. Feteira, Q.L. Zhao, X.L. Tan, I.M. Reaney, *J. Mater. Chem. A* **6**, 4133 (2018)
33. D.W. Wang, Z.M. Fan, W.B. Li, D. Zhou, A. Feteira, G. Wang, S. Murakami, S.K. Sun, Q.L. Zhao, X.L. Tan, I.M. Reaney, *A.C.S. Appl. Energy Mater.* **1**, 4403 (2018)
34. D.W. Wang, G. Wang, S. Murakami, Z.M. Fan, A. Feteira, D. Zhou, S.K. Sun, Q.L. Zhao, I.M. Reaney, *J. Adv. Dielectr.* **8**, 1830004 (2018)
35. L.Y. Zhang, Z.Y. Wang, Y. Li, P. Chen, J. Cai, Y. Yan, Y.F. Zhou, D.W. Wang, G. Liu, *J. Eur. Ceram. Soc.* **39**, 3057 (2019)
36. L.J. Liu, D.P. Shi, M. Knapp, H. Ehrenberg, L. Fang, J. Chen, *J. Appl. Phys.* **116**, 184104 (2014)
37. L.J. Liu, M. Knapp, H. Ehrenberg, *J. Eur. Ceram. Soc.* **37**, 1387 (2017)
38. G.Z. Dong, H.Q. Fan, J. Shi, M.M. Li, *J. Am. Ceram. Soc.* **98**, 1150 (2015)
39. G.Z. Dong, H.Q. Fan, J. Shi, Q. Li, *J. Am. Ceram. Soc.* **101**, 3947 (2018)
40. Q. Li, Z.J. Yao, L. Ning, S. Gao, B. Hu, G.Z. Dong, H.Q. Fan, *Ceram. Int.* **44**, 2782 (2018)
41. C. Ang, Z. Yu, *Appl. Phys. Lett.* **95**, 232908 (2009)
42. M. Vögler, N. Novak, F. Schader, J. Rödel, *Phys. Rev. B* **95**, 024104 (2017)
43. J.J. Yao, L. Yan, W.W. Ge, L. Luo, J.F. Li, D. Viehland, Q.H. Zhang, H.S. Luo, *Phys. Rev. B* **83**, 054107 (2011)
44. X. Lai, H. Hao, Z. Liu, S. Li, Y. Liu et al., *J. Mater. Sci.-Mater. Electron.* (2020). <https://doi.org/10.1007/s10854-020-03430-7>
45. D.D. Han, C.H. Wang, D.Y. Lu, F. Hussain, D.W. Wang, F.L. Meng, *J. Alloys Compd.* **821**, 153480 (2020)
46. W.M. Xia, Y.M. Liu, G. Wang, J.L. Li, C.J. Cao, Q.Y. Hu, Y.Q. Chen, Z.L. Lu, D.W. Wang, *Ceram. Int.* **46**, 2954 (2020)
47. D.W. Wang, D. Zhou, K.X. Song, A. Feteira, C.A. Randall, I.M. Reaney, *Adv. Electron. Mater.* **5**, 1900025 (2019)
48. J.N. Sui, H.Q. Fan, B. Hu, L. Ning, *Ceram. Int.* **44**, 18054 (2018)
49. B. Hu, H.Q. Fan, L. Ning, S. Gao, Z.J. Yao, Q. Li, *Ceram. Int.* **44**, 10968 (2018)
50. M. Acosta, J.D. Zang, W. Jo, J. Rödel, *J. Eur. Ceram. Soc.* **32**, 4327 (2012)
51. H.L. Cheng, H.L. Du, W.C. Zhou, D.M. Zhu, F. Luo, B.X. Xu, *J. Am. Ceram. Soc.* **96**, 833 (2013)
52. R. Dittmer, W. Jo, D. Damjanovic, J. Rödel, *J. Appl. Phys.* **109**, 034107 (2011)
53. F. Yang, L. Li, P. Wu, E. Pradal-Velázquez, H.K. Pearce, D.C. Sinclair, *J. Mater. Chem. C* **6**, 9258 (2018)

**Publisher's Note** Springer Nature remains neutral with regard to jurisdictional claims in published maps and institutional affiliations.